Scalable Thermoset Informatics and On-Demand Discovery through Autonomous Experimentation

Marcus R. Fratarcangeli,[1†] Ayush Jain,[2,3†] Farzad Gholami,[1,2†] Jiaqi Nie,[1] H. Jerry Qi,[1*] and Rampi Ramprasad[2*]

[1]School of Mechanical Engineering, Georgia Institute of Technology, Atlanta, GA 30332, United States

[2]School of Materials Science and Engineering, Georgia Institute of Technology, Atlanta, GA 30332, United States

[3]School of Computational Science and Engineering, Georgia Institute of Technology, Atlanta, GA 30332, United States

†Equal Contribution First Authors

*Corresponding authors, HJQ, qih@me.gatech.edu; RR, rampi.ramprasad@mse.gatech.edu

Abstract

As photo-polymer additive manufacturing matures, there is an increasing need for on-demand, application-specific materials. A major bottleneck is the limited exploration of the vast design space for new thermoset polymer formulations, which must satisfy both material property requirements and processing constraints. This challenge stems from the combinatorial complexity of possible formulations and the high cost of experimental evaluation. In this work, we present an end-to-end pipeline that integrates a self-driving laboratory (SDL) with informatics-driven optimization to discover and validate novel thermoset acrylate formulations. The pipeline starts with a database focusing on thermoset acrylates that consolidates multiple data sources (including manual and SDL experiments, molecular dynamics simulations, and literature data). Selected datasets are used to train both single-task and multitask predictive models, which interface directly with our SDL platform to measure mechanical and processing-related properties. Each component of the pipeline is validated independently and then deployed together to optimize a target elastomeric material in significantly less time and with substantially reduced human effort. This work establishes a scalable framework for embedding multi-fidelity machine learning tools within laboratory workflows, paving the way for the next generation of autonomous, data-driven thermoset formulation discovery for additive manufacturing.

Keywords: Self-driving laboratory; additive manufacturing; 3D printing; material informatics; photopolymers.

1 Introduction

Photocurable acrylates are a cornerstone of additive manufacturing (AM),[1] particularly in vat photopolymerization techniques such as digital light processing (DLP), which enable the rapid fabrication of complex structures.[2,3] The versatility of acrylate chemistry, which enables network formation from diverse monomers and crosslinkers, opens a vast, largely unexplored compositional space.[4,5] This offers the potential to create bespoke materials with precisely tailored mechanical, thermomechanical, and processing properties on a per-need basis. However, the current selection of validated photopolymer resins for AM is narrow, forcing compromises for downstream production.[6]

Although machine learning (ML) offers a powerful route for exploring the vast design space of homopolymers,[7,8] copolymers,[9] and blends,[10] thermosets and acrylates have not been explored at scale. The primary obstacle to expanding this material library is the experimental effort required and the processing parameters to control (i.e., UV light intensity, time of light exposure, and environmental temperature). Active learning (AL) helps reduce this burden by efficiently guiding experiments,[11] but its impact is limited by experimental throughput. Automation through self-driving laboratories (SDLs) can overcome this challenge, enabling high-throughput formulation and characterization.[12-15] Equally important is the integration of diverse data sources through multi-task[16] and multi-fidelity learning,[17] which unifies experimental, simulated, and literature data. Together, these advances accelerate discovery and establish a scalable framework for data-driven materials innovation.

In this work, we present an end-to-end pipeline embedded directly into an SDL for the on-demand discovery of thermoset acrylate resins that target desired mechanical properties. As shown in **Figure 1**, our pipeline starts with data integration (**Figure 1a**) from the SDL, manual experiments (from our earlier work), molecular dynamics simulations,[18] as well as the collection of literature experiments into a database designed for thermoset polymers, *ThermosetDB* (**Figure 1b**). The data is then used in informatics tools to build models for predicting the properties of future thermoset formulation candidates (**Figure 1c**). Finally, we use the models for Bayesian and Gradient-based optimization (**Figure 1d**), which interface directly with the SDL. The SDL receives candidates and automates the creation of samples, testing of processing variables and mechanical properties (**Figure 1e**). The new data is uploaded back to *ThermosetDB*, and is used to retrain models for future optimization. We demonstrate the use of this framework to optimize an elastomeric material with up to 90% reduced human time in experimentation and formulation trials. The informatics pipeline, combined with diverse chemical data and connection to the SDL, creates a scalable and chemically flexible framework to accelerate the discovery of high-performance, photocurable acrylates for next-generation additive manufacturing.

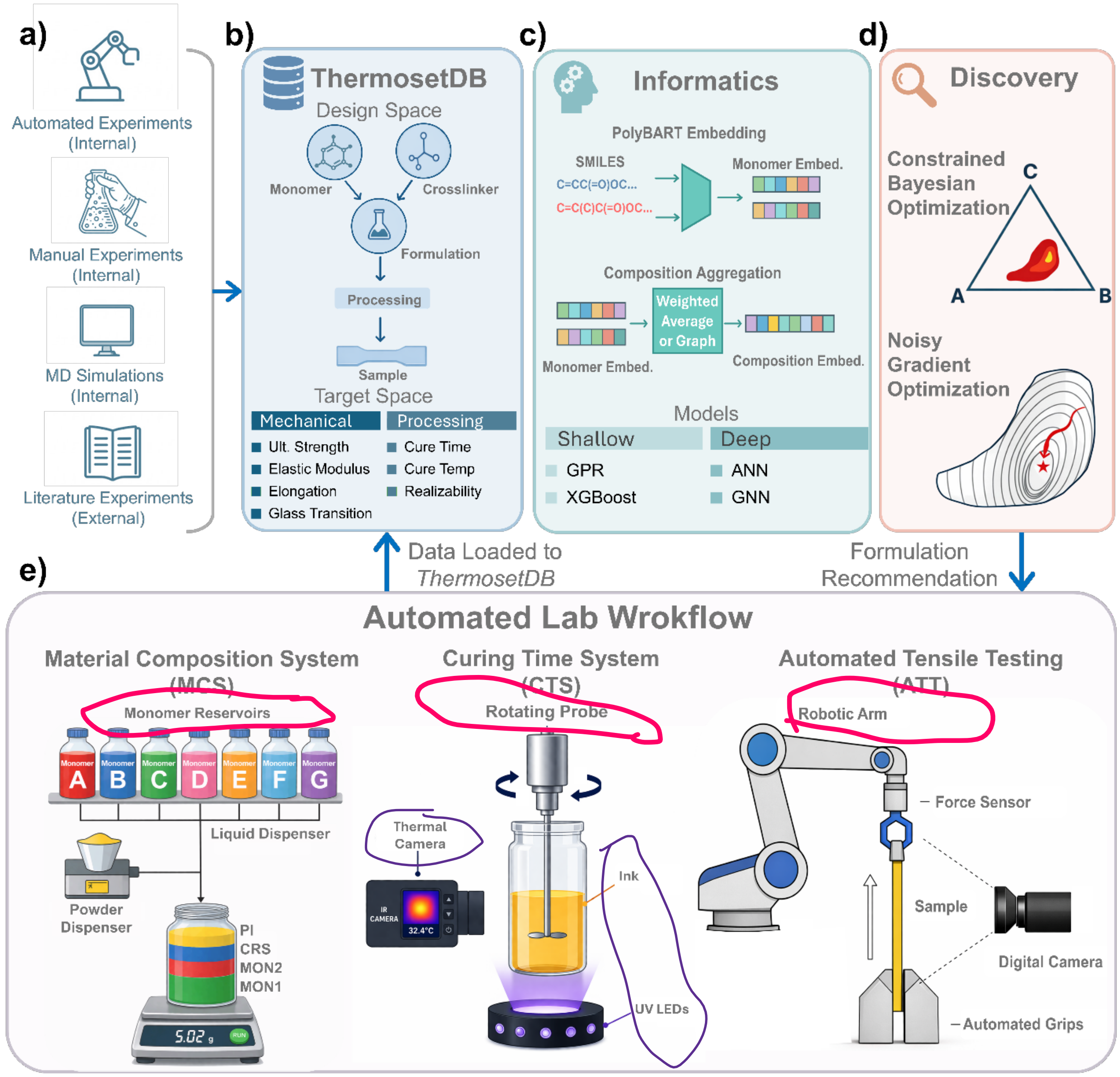

Figure 1. Overview of the end-to-end thermoset informatics pipeline. a) Data from multiple sources, including SDL and manual experiments, molecular dynamics simulations, and literature experiments. b) Setup of the *ThermosetDB* database schema to respect the multi-step processing conditions that create thermosets. c) Informatics of thermosets through the use of the polyBART embedding for monomers. These embeddings can be used in a mixture of shallow and deep models. d) Acceleration of new formulations using Bayesian and Gradient optimization methods. e) The SDL setup, which utilizes the recommendations from informatics. The SDL consists of 3 phases: formulation creation via the Material Composition System (MCS), processing property determination through the Curing Time System (CTS), and mechanical property characterization via Automated Tensile Testing (ATT). The data collected is fed back into *ThermosetDB*.

2 Methodology

2.1 Experimental Methods

2.1.1 Self-Driving Lab Architecture

Our SDL system contains three primary components (**Figure 1e**): processing, characterization, and decision making.[19] The layout of the SDL hardware is shown in Supplementary Information Section 6. First, the processing system is labeled as the Material Composition System (MCS), which automatically dispenses and mixes photopolymer inks. In addition, the fabrication of tensile bars is included in the processing component. Second, the characterization of the photopolymer inks is divided into two subsystems: the curing time system (CTS) and the automated tensile testing system (ATT). The CTS tests the curing time and temperature rise during curing. It then determines the realizability of the inks, which is defined that curing time and temperature rise must fall within certain thresholds for the ink to be considered usable for DLP printing). The ATT provides the modulus of elasticity, ultimate tensile strength (UTS), and elongation at break. Third, the decision-making component (**Figure 1a-d**) contains the active learning algorithm, which takes the CTS and ATT results and then provides several recommendations (four in this work) for next photopolymer compositions to test. The recommended compositions are then passed to MCS to start a new iteration.

Material Composition System: The MCS comprises two primary components: the monomer liquid dispenser and the photoinitiator powder dispenser. In this work, the MCS is limited to a total number of nine types of monomers due to physical constraints. The monomer liquid dispenser consists of a series of peristaltic pumps powered by stepper motors.[20] The step speed determines the amount of liquid dispensed; therefore, a proportional integral derivative (PID) control algorithm is implemented for accurate dispensing. During dispensing, the container is placed on a scale where the dispensing nozzles are overhead, and the scale reading is continuously monitored as feedback. The scale resolution is 0.003 grams; compared to the total amount of dispensed liquid of 8 grams, this is more than sufficient to minimize error in the early stages of the SDL. The photoinitiator powder dispenser similarly uses a stepper motor, which is connected to a pinion that turns a spur gear with a through hole on its face. There is a funnel containing the photoinitiator, aligned with the circular path of the spur gear hole. As the funnel exit aligns with the hole, the powder is dispensed and incentivized by a vibrating motor attached to the funnel. The revolution speed as well as the number of revolutions determine the amount of photoinitiator dispensed. Sampling the speed and mass spaces allows a curve fit between gear speed and dispensed mass, which can then be used to interpolate the required speed for any desired mass. Besides the two dispensing systems, the MCS also contains a robotic arm with a custom gripper that facilitates the movement of the ink container between the liquid dispenser, powder dispenser, and mixer. Finally, a magnetic mixer is used to mix the inks after all the components are dispensed. A video demonstration of a complete loop of the MCS is included in the Supplementary Information (**Movie S1**).

Curing Time System: For a photopolymer resin to be realizable for 3D printing, its curing time should fall within a reasonable range. In addition, the temperature rise during curing cannot be too high. Although both curing time and temperature could be subjective, we use 10s and 70ºC, respectively, in this work. Our assumption of designing the CTS is based on two features of photocuring. First, the photopolymerization reaction is exothermic.[21] Therefore, as the resin is cured, it is expected that the temperature will rise. Second, when the resin is cured from a liquid state to a solid state, its viscosity will increase, which can be detected through the change of a torque while stirring the ink. Based on these two assumptions, we designed the hardware comprising a robotic arm and a thermal camera. The robotic arm () has a built-in torque sensor and an electromechanical servo gripper that places a probe into the photopolymer ink. The data collection process begins with the robot wrist rotating slowly and turning the probe. At the same time, a thermal camera records the temperature of the ink. The UV LED lights are then turned on to begin the reaction. Both the torque and temperature are measured to determine the curing properties of each photopolymer ink through an automated data analysis process. A video demonstration of CTS data is included in Supplementary Information (**Movie S2**). Typical temperature and torque evolution curves are presented in **Figure S5** and **Figure S6**, respectively.

Automated Tensile Testing System: The second system for characterization is for mechanical properties. The samples are first manually cured into dog-bone tensile bars in accordance with ASTM D638 Type V for polymer materials (with a total length of 63.50mm and a gauge length of 9.53mm).[22] These samples are then placed on a rack for ATT for testing. The ATT system consists of a robotic arm with an electromechanical servo gripper (the same one used in the CTS), which works with an in-house-built automated clamp to secure the tensile bars from the bottom as the tensile testing frame. The force is measured by the built-in force sensor. In addition, the robotic arm is equipped with a position tracking system, which continuously records its spatial position during the tensile test. During a tensile test, the robotic arm grabs one end of a sample from the rack, then moves it and inserts the other end into the automated clamp, which then closes and secures the sample from the bottom. The robotic arm then moves vertically up by 60mm at a displacement rate of 1 mm/s. Once the robotic arm reaches 60mm of travel, the bottom clamp opens. The robotic arm then moves to the sample damping area, opens its grip, and moves against a fixed brush to ensure the tested sample is brushed off. It then grabs another brush to clean the bottom clamp. This finishes one tensile test. During the test, the sample dimensions are measured using digital image correlation (DIC) with two digital cameras.[23,24] The ATT system also takes the force and dimension to automatically obtain the stress and strain curve and extract mechanical properties, including the modulus of elasticity, ultimate tensile strength (UTS), and elongation at break. A video demonstration of ATT tests is shown in the Supplementary Information (**Movie S3**)

Since the SDL will conduct tests autonomously, an area of concern in automated testing is verifying test integrity and detecting contingencies for anomalous activity. In tensile testing, samples may contain defects and fail prematurely or break in an unexpected or undesirable manner. Therefore, an anomaly detection model consisting of two convolutional neural networks (CNNs) for the front and side views of the sample was developed to analyze and classify the breakage point of samples after a tensile test. A dataset of 660 images was collected from the front and side cameras after tensile tests, where each frame was labeled as one of four classes: gauge break, low break, high break, sample stretched, with a split of 29.2%, 28.0%, 30.1%, and 12.7%, respectively. The gauge break implies the tensile bar broke within the gauge region, high break means the sample broke above the gauge region, low break means below the gauge region, and sample stretched means the sample did not break at all. The dataset was split 90/10 for training and validation, and frames were cropped to 600x250 pixels and normalized before processing to reduce noise. Each CNN contained four convolutional layers with 7x7, 5x5, 3x3, and 3x3 kernels, respectively, and was trained using the *AdamW* optimizer and learning rate optimizer for 35 epochs. The final model uses the mean predictions from both the front and side CNNs to select the final class.

2.1.2 Manual Characterization Techniques

The glass transition temperature (T_g) of the samples was determined by dynamic mechanical analysis (DMA) using a Q800 instrument (TA Instruments, New Castle, DE, USA). A temperature ramp of 5 ℃ per min was applied while oscillating the samples at 1 Hz with 0.1% strain. T_g values were extracted from the maximum of the tan δ signal, corresponding to the transition from the glassy to the rubbery state. The degree of conversion was determined by normalizing the FTIR peak intensity corresponding to the acrylate group at 809 cm^{-1}, measured using a Nicolet 6700 spectrometer (Thermo Fisher Scientific, Waltham, MA, USA). Three measurements were performed for each sample to ensure reproducibility.

2.2 Informatics Methods

2.2.1 Thermoset Fingerprinting

The state of the art in polymer fingerprinting is largely driven by tools such as Polymer Genome[25] and a range of graph-[8] or language-based models.[26] These approaches are primarily designed for linear polymers. However, such formulations do not naturally extend to thermosets, where monomers can have multiple reaction sites, enabling the formation of crosslinked networks. To address this limitation, we conceptualize thermoset polymers as mixtures or formulations of fingerprints corresponding to the monomers that form the network. We use *polyBART*, an encoder-decoder based framework that has been trained on SELFIES representations of polymers and molecules,[27] to create embeddings of monomers. We represent the thermoset as an aggregation of the individual parts (Figure 1C). The most intuitive way for this aggregation can be through a weighted average *F* of the fingerprints of each constituent f_i as shown in **eq. 1**,

$$F = \frac{1}{N}\sum_{i}^{N} m_i f_i \tag{1}$$

where m_i is the molar ratio of the specific composition.

However, the influence of different monomers is not determined solely by their molar ratios, but also by their functionality. For example, poly(ethylene glycol) diacrylate (PEGDA), a crosslinker with 2 functional groups, may exert a greater influence on the physical properties of thermosets compared to a monomer such as glycidyl methacrylate (GMA), which has only one functional group. Thus, a fingerprinting method must account for the impact of each component being dependent on the other components in the formulation. For this reason, we derived a *reaction-graph-based*[28] approach to fingerprinting thermosets, explicitly incorporating reactivity and connectivity patterns into the representation to better learn the structural and functional complexity of cross-linked polymer networks from the composition ratios. Each molecular reaction system is represented as a graph $G = (V, E)$, where V denotes the set of nodes (atoms or molecular fragments) and E denotes the set of edges, which are the sets of reactions that occur. This is a fully connected graph. Each node $i \in V$ is associated with an initial feature vector $x_i \in R^{d_{in}}$ encoding atomic or fragment-level descriptors. The nodes are fully connected with loops. Node-representation $h_i = contat([x_i, f_i])$ where f_i is the mole fraction of the monomer. A multitask graph neural network (GNN) is used to learn a latent aggregation of the thermoset features and predict final properties (elaborated in Supplementary Information Section 2).

2.3 Molecular Dynamics Simulation Methods

Glass transition temperatures were calculated through cooling simulations using the CHARMM force field[29] in GROMACS.[30] The thermoset systems were created by starting with the monomers in a periodic simulation box at an initial density of between 250 to 350 g/cm^3. 21-step equilibration was performed on the system, with a “mixing” step at 700K to ensure the monomers were evenly distributed. After equilibration, iterative curing cycles were conducted by finding nearby reactive acrylate functional groups, dragging them together, adding a bond to the topology, and then relaxing the system.[31] This process was continued iteratively until the desired conversion rate was reached. The cured systems were energy minimized (10,000 steps, steepest descent), pre-annealed under constant-temperature, constant-pressure ensemble (NPT) conditions (2,000 ps, 500 K, 10.0 bar, 0.001 ps timestep) to bring the density to a favorable amount if needed. Following a 21-step equilibration ending at 650 K, systematic cooling was performed from 650 K to 75 K in 30 K decrements. At each temperature point, a two-stage protocol was employed: (1) NPT annealing with controlled linear cooling over 6,000 ps at 1.0 bar, and (2) isothermal NPT production at the target temperature for 5,000 ps. Timesteps were adaptively set to 0.001 ps for $T < 250\ K$ and 0.0005 ps for higher temperatures. This allowed for stability during high vibrational activity but remained efficient when not necessary. System temperature and volume were monitored throughout each production run. The resulting volume vs. temperature data was fitted using a hyperbolic function[32] (elaborated in Supplementary Information Section 2) to determine the transition interval T_{low} to T_{high} where the T_g lies. Separate linear fits were performed on the low-temperature and high-temperature regions. Data points where $T < T_{low}$ are fit to a linear function are considered the low temperature region and data points where $T > T_{high}$ are fit to a linear function are considered a high temperature region. The T_g is determined as the intersection point of the two linear fits from the low-temperature and high-temperature regions. To ensure validity, we compute R^2 values for a general hyperbolic fit applied to the complete dataset, a linear fit applied to the low-temperature segment, and a linear fit applied to the high-temperature segment.

2.4 Optimization Methods

2.4.1 Bayesian Approach

The Bayesian optimization (BO) approach followed a scaled-up protocol to our previous work of machine-guided design in acrylates.[11] A 7-dimensional design space was divided into increments of 5% weight ratios. We enumerated a candidate space of compositions with up to three components. The crosslinker ratios were capped to 50% so that the crosslinking did not overtake the properties of composition. The surrogate model is trained on previous trial data, and predicts on the candidate space. Unlike much of the theoretical work in multi-objective BO, materials design spaces are not smooth functions to estimate, but noisy functions with “islands” of different phases and realizability. The acquisition criteria are not always a maximization or minimization, and can include numerical targets, or ranges of satisfactory property values. To this end, a composite acquisition function is used to evaluate suitable candidates. Three distinct categories of design targets comprise this acquisition function, each having its own scoring given a candidate x and its posterior mean $\mu(x)$ and standard deviation $\sigma(x)$:

- **Maximize or Minimize**: 1D Expected Improvement (EI)[7,33] formulation is used. Given the best observed value in the current dataset, the acquisition is computed as **eq. 2**:

$$EI(x) = \begin{cases} \alpha(\mu - f_{best})\Phi(z) + (1-\alpha)\sigma\phi(z), & \text{for maximization} \\ \alpha(f_{best} - \mu)\Phi(z) + (1-\alpha)\sigma\phi(z), & \text{for minimization} \end{cases} \tag{2}$$

where $z = \frac{|\mu - f_{best}|}{\sigma}$, Φ and ϕ are CDF and PDF of the standard normal distribution, and α balances exploitation and exploration.

- **Target**: The predictive distribution is transformed into a Gaussian function centered at the desired target value f^*. For each candidate, samples are drawn as $f(x) \sim N(\mu(x), \sigma^2(x))$ and their squared deviation from the target $(f(x) - f^*)^2$ is computed. The distribution of this value can be framed as a minimization problem (the deviation decreases as $f(x)$ gets closer to f^*). Then, the EI is computed using the minimization form above. This formulation rewards candidates whose posteriors overlap with regions around f^*.
- **Range**: This can be interpreted as adding constraints to the search by calculating the probability $\left(P_{range}(x)\right)$ of the posterior distribution falling into the desired range $[L, U]$. If the criteria have no lower bound (ex. a property only needs to be $< U$), then $L = 0$. If the criteria have no upper bound (ex. a property only needs to be $> L$), then $U = \infty$. Formally, this is defined as **eq. 3**,

$$P_{range}(x) = P(L \leq f(x) \leq U) = \Phi\left(\frac{U - \mu(x)}{\sigma(x)}\right) - \Phi\left(\frac{L - \mu(x)}{\sigma(x)}\right) \tag{3}$$

as more of the distribution falls into the desired range the score will be higher.

An acquisition superscore can be given to candidates by taking an importance-weighted average of individual property scores, $\sum_{i=1}^{N_{var}} \omega_i \mathrm{A}_i(x)$, where $\mathrm{A}_i(x)$ is the objective acquisition score, and ω_i is a given weight (default is 1.0) for the i^{th} target.

2.4.2 Gradient Approach

() Gradient optimization is used to find compositions when a neural network architecture is trained on sufficient data from many sources, allowing a design space search that is not limited to enumeration. In this case, we use the multi-task GNN and reaction graph approach. The optimization traverses the formulation simplex (a space where every point sums to 1) to find a composition of n components $x = [x_1, x_2, \ldots, x_n]$ that minimizes a multi-objective loss function $\mathcal{L}$ as shown in **eq. 4**,

$$\min_x \mathcal{L}(x) = \sum_{k=1}^{K} \omega_k \mathcal{L}_k(f_k(x), t_k) \tag{4}$$

where $f_k(x)$ denotes the GNN-predicted property k, t_k is target value or range, ω_k is a property-specific weight, and K is the number of properties under consideration. $\mathcal{L}_k$is deviation of each goal from the target. From a starting point, which is a noised composition from the Bayesian step, we complete 10 forward passes through the GNN model using Monte Carlo dropout. $\mathcal{L}$ is calculated and the gradients of $\mathcal{L}$ with respect to the composition, $\frac{\partial \mathcal{L}}{\partial x}$, is calculated via auto-differentiation. A modified, simplex-aware Adam optimizer steps x. This process is repeated multiple times until $\mathcal{L}$ converges. Through the iterations, sparse components are pruned dynamically from the graph representation, and we use randomized Dirichlet sampling at premature conver-gences to escape local minima. Further details of this procedure, including relevant equations, are available in Supplementary Information Section 3.

2.4.3 Regret Calculation

Regret quantifies the deviation of the measured property values from their desired targets. A higher regret indicates that the sample is further away from the target. For a property p with observed value x_p and target t_p, the normalized per-property regret is defined as **eq. 5**:

$$r_p = \begin{cases} \dfrac{\left(x_p - t_p\right)^2}{max_i(x_{p,i} - t_p)^2}, & \text{if } t_p \text{ is a scaler target} \\ \dfrac{\max(0, t_p^{low} - x_p, x_p - t_p^{high})^2}{max_i r_{p,i}}, & \text{if } t_p \text{is a range target} \left[t_p^{low}, t_p^{high}\right] \end{cases} \tag{5}$$

The total regret for a sample is computed as the summation over all goal properties, $R = \sum_p r_p$.

3 Results and discussion

3.1 Self-Driving Lab Performance

The SDL was used to conduct automated tests with the integrated active learning loop described above. Here, we used 9 monomers. The system was tested by 18 generations. In each generation, four compositions were tested. For each composition, it was mixed once by MCS, three were tested by CTS, and eight were tested by ATT. To evaluate the SDL's performance, we compared its time metrics of manual experimentation versus the actual human effort required to operate the SDL. Note that there are some tasks that need human work in SDL, such as loading raw materials and containers, placing probes, preparing tensile samples, and placing the samples onto the rack.

Table 1 summarizes the acceleration achieved in the photopolymer data collection process per iteration while **Table 2** shows the overall efficiency metrics of the system. In Table 1, the time values correspond to the duration of running each system for a single iteration in our optimization loop, which consists of four compositions. Here, human time refers to the length of time during which a researcher must be actively present and working with the SDL for tasks mentioned above. The SDL reduces human time requirements by 91.3%, freeing more than six hours of a typical workday for other research activities. Furthermore, the previously time-intensive task of manual data analysis for both characterization systems is now fully automated, achieving a 100% reduction in manual analysis time.

Table 1 Acceleration of experimental procedures via the SDL

Metric	SDL run time (min)	Human time (min)	Manual time (min)	Human time saved* (%)
Photo-polymer Processing	60	5	40	87.5
Curing Time Testing	48	10	60	83.3
Tensile Testing	160	20	180	88.9
Data Analysis	0	0	120	100
Total	268	35	400	91.3

* Human time saved = $\left(\frac{t_{manual}-t_{human}}{t_{manual}} * 100\right)$

Table 2. Efficiency metrics of the SDL

Metric	Value	Material Composition System	Curing Time System	Automated Tensile Testing
Time per sample (min)	t_s	15	4	5
Samples per composition	s_c	1	3	8
Samples per iteration	s_i^*	4	12	32
Time per iteration (min)	t_i^{**}	60	48	160

$^* s_i = s_c \times 4$, $^{**} t_i = t_s \times s_i$

Figure 2 demonstrates the verification of the SDL systems. The MCS liquid dispensing system was tested by dispensing monomers at various target masses to verify the precision and accuracy of the system, while also finding the resolution as shown in **Figure 2a**. The results clearly show the system efficacy and minimization of error early in the SDL stages. **Figure 2b** shows the relationship between the cure time measured in the CTS and DLP printer. This model was utilized to map the tested photopolymer inks cure times to validate their use in DLP printing. Last, **Figure 2c** illustrates the ATT system tensile data results compared to an MTS Criterion machine. The same samples were tested in both machines by stretching the samples to 300% strain and then allowing them to relax. The results show strong similarities between the material behavior, indicating the effectiveness of the ATT. The anomaly detection model utilized in the ATT demonstrated consistent accuracy in identifying the breakage point of tensile bar samples. In the validation set, the front and side CNNs achieved average F1 scores of 0.96 and 0.94, respectively.

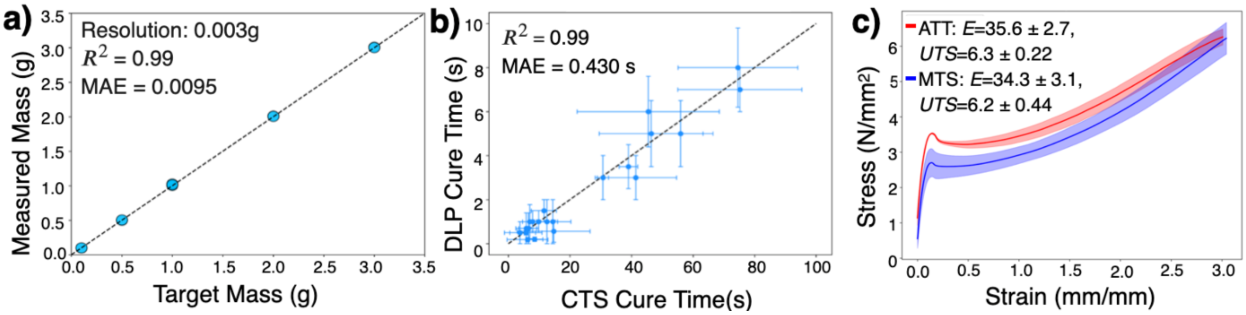

Figure 2. Accuracy of each part of the SDL. a) Parity plot of the measured mass of the Material Composition System (MCS) vs. the target mass. b) Scaled parity plot of the measured curing time from the Curing Time System (CTS) vs. the true cure time. c) Comparison of the stress strain curves of a thermoset from Automated Tensile Testing (ATT) and the MTS.

3.2 Acquired Datasets

In this work, we collected data from in-house experiments (both manual and via SDL), the literature, and synthetically generated molecular dynamics simulations. For literature experiments, we constrained the collection to neat acrylate thermosets cured via UV radiation,[4,5,34-41] with no reduction in the deviation of signals in the dataset from dissimilar processing techniques. **Figure 3** shows the summary of chemical and property distributions of literature and in-house experiments. In **Figure 3a**, in-house experiments are limited to a few main monomers accessible to our lab, and literature experiments include a diverse set of monomers. Supplementary Information Section 1 contains the string representation (Simplified Molecular Input Line Entry System) of the acrylate monomers and crosslinkers considered across all datasets. In **Figure 3b**, we see that experiments are more clustered in the chemical space as the monomers used are limited to those available in our lab. With literature data sets, we can expand to more diverse chemical spaces while including some overlap between literature and in-house.

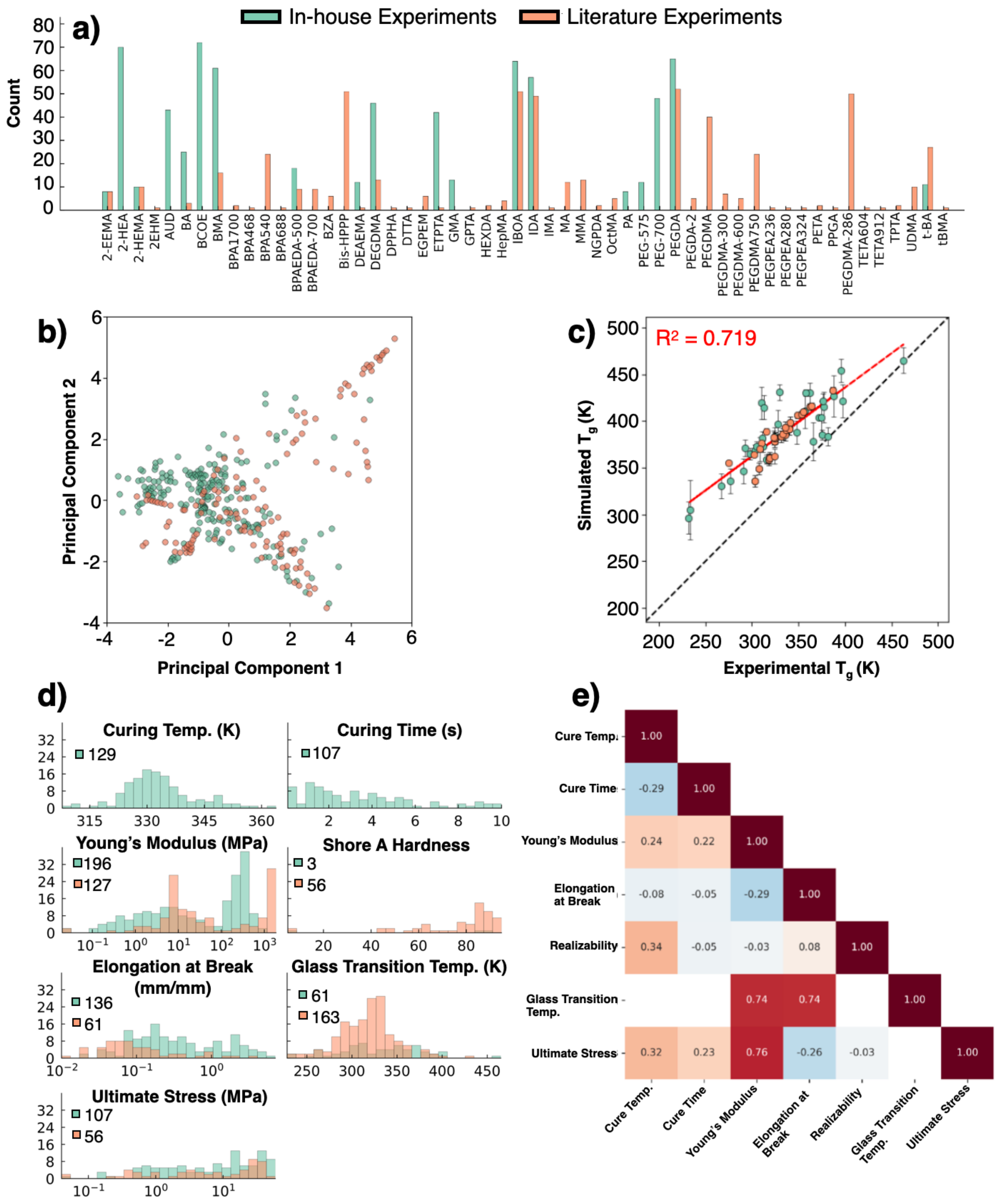

Figure 3. Data within ThermosetDB for both in-house (green) and literature experiments (orange). a) Distribution of compositional occurrences in experimental datasets. b) Visualization of the chemical-space based on compositional embeddings of the formulations after PCA reducing to 2 dimensions (46% total variance). c) [QJH23.1]The glass transition temperature simulation alignment with in-house and literature experiments. d) Property distributions from experimental data along with the in-house experiment and literature experiment counts. e) Property correlations with experimental data in the in-house data points.

Classical MD simulations have been used to simulate thermomechanical properties for linear polymers[42] and thermosets,[43] focusing on epoxies. In **Figure 3c**, we show simulated T_g values in comparison with both literature and in-house experiments. We conduct three trials per formulation, each with a different crosslinked configuration. MD simulations were performed only for values where the conversion percentage was reported. For any compositions with ranges of conversions, we linearly interpolate to estimate the T_g at intermediate conversions. The T_g calculated values from simulations are generally higher than those found experimentally. This is expected, as the time scales for simulation are much shorter, so the polymer chains do not have time to relax and end up in a less ideal configuration, causing a higher observed transition point. Because this is a time scale problem, a correction factor can be estimated. The observed average difference between simulated and experimental T_g values is 58.3 K, corresponding to an estimated shift of ~5.3 K per order of magnitude in cooling rate. The corrected simulation values have an r^2=0.719. Additionally, we see that using the conversion percentage can align the measurements from different data sources as it unifies the results of processing variations across literature.

Despite these high-level trends being simulated, there are shortcomings of the current simulation approach. The three crosslinked samples represent only a small subset of the possible network structures. Consequently, results based on only three trials may be influenced by non-representative network configurations. Additionally, the use of a classical force field introduces limitations, as its accuracy may vary across monomers. The true potential of this approach lies in integrating simulations with experimental datasets within our informatics framework, which we explore in the subsequent section.

Figure 3d summarizes the collected property values for both in-house experiments and literature data. Our in-house experiments include a greater proportion of softer thermosets, with $E < 1\ GPa$ and a high percentage of samples showing an Elongation at Break of $>$ %, whereas literature highlights stiffer materials. This distribution will continue to evolve as materials are developed for increasingly diverse application needs and as the set of in-house experimental monomers expands. **Figure 3e** highlights correlations between collected property values, justifying further use of multi-task modeling. The glass transition temperature, Young's modulus, elongation at break, and ultimate stress hold strong correlations between each other. The resulting database provides a scalable backbone for the closed-loop optimization framework, enabling the training and benchmarking of machine learning methods, including the multitask models that drive optimization. By integrating in-house experimental data with literature sources, this approach also supports the flexible expansion of the accessible design space in future work.

3.3 Benchmarking of Machine Learning Models

As informatics at scale for acrylate thermosets is a gap in materials literature, it is important to benchmark the use of different fingerprinting and machine learning models. We compare several strategies, including a graph-based aggregation and a molar ratio weighted average aggregation. In the first approach, the GNN learns a fingerprint from monomer features and their molar ratios and predicts properties with a fully-connected head. In the second approach, we use an artificial neural network (ANN), Gaussian process regression (GPR), and XGBoost (XGB) with the pre-combined fingerprint. We seek to validate the use of multiple data sources on model accuracy, similar to work conducted for homopolymers. We present model training over single-task (ST) datasets (one property from our in-house experiments), multi-fidelity (MF) datasets (one property but combining in-house experiments and literature data), and multi-task (MT) datasets (all properties are learning as different tasks). All dataset variations used in this study are retrieved from the curated thermoset database described above.

An important consideration is that the degree of curing, or conversion percentage from monomer to thermoset, greatly influences the properties.[18,21,27] In theory, this conversion could be used as a predictive feature for property modeling. However, accurately measuring it requires infrared spectroscopy of both cured and uncured samples.[18] This adds another layer of experimental effort, reducing the returns of adding this feature. Therefore, we train our models only on thermosets that have reached the conversion level at which polymerization stops. This value inherently depends on composition, so using the maximum attainable conversion provides a practical balance between model accuracy and experimental efficiency.

Table 3. Model performance across target properties.

Model	RMSE↓						r^2 ↑					
	E (log MPa)	**T_g (K)**	**Max Strain (log mm/mm)**	**Ult. Stress (MPa)**	**Cure Time (s)**	**Cure Temp (K)**	**E**	**T_g**	**Max Strain**	**Ult. Stress**	**Cure Time**	**Cure Temp**
GNN_MT_MF	0.55	30.1	0.34	0.30	2.26	6.98	0.76	0.56	0.67	0.83	0.20	0.44
ANN_MT_MF	0.56	34.4	0.36	0.29	2.02	7.65	0.74	0.43	0.61	0.84	0.01	0.33
GRN_MT_MF	0.62	31.2	0.44	0.43	2.26	7.02	0.69	0.53	0.43	0.66	0.24	0.43
XGB_MT_MF	0.73	34.5	0.49	0.47	2.16	7.40	0.56	0.43	0.27	0.60	0.17	0.38
GNN_ST	0.59	43.3	0.33	0.46	2.05	7.64	0.71	0.10	0.69	0.59	0.34	0.32
ANN_ST	1.32	59.7	0.34	0.31	2.06	7.91	-0.39	-0.7	0.67	0.81	0.34	0.28
GRN_ST	0.62	40.6	0.43	0.42	2.10	7.74	0.69	0.21	0.47	0.67	0	0.31
XGB_ST	1.08	63.7	0.37	0.46	1.93	7.16	0.05	-0.9	0.59	0.59	0.45	0.40

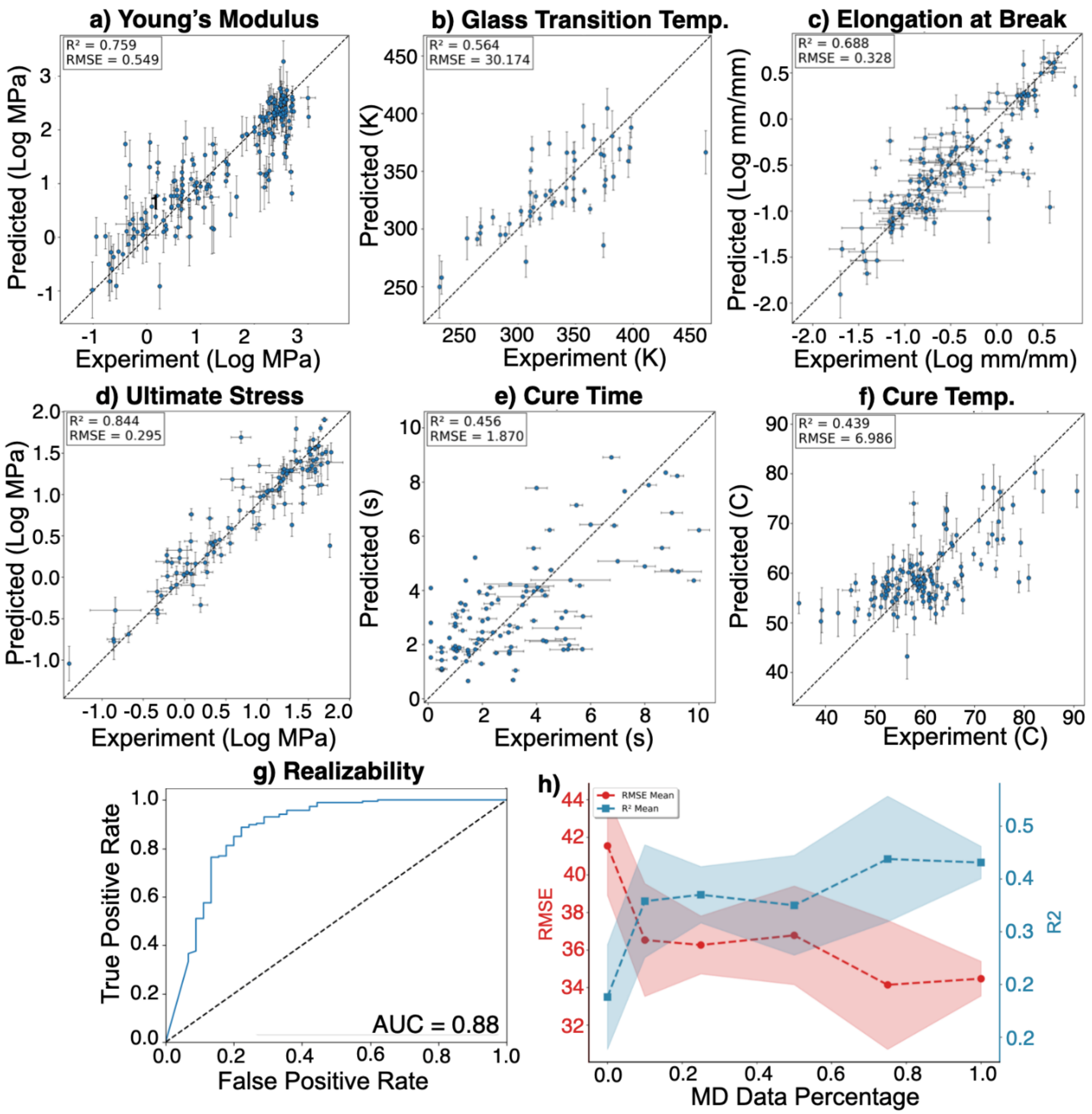

Figure 4.Results of selected best informatics benchmarks, aligned with the models high-lighted in 3. a) E parity of GNN MT MF. b) Tg parity of GNN MT MF. c) max strain parity of GNN ST. d) UTS parity of ANN MT MF e) Cure Time parity of GPR MT MF. f) Cure Temperature parity of GNN MT MF. g) Receiver Operating Characteristic of Realizability predictions from a ANN ST. h)The RMSE and $R^2$of the glass transition temperature predictions across different amounts of molecular dynamics (MD) data in the train set.

In **Table 3** we show the model performance through the root mean squared error (RMSE) and linear correlation coefficient (r^2) between the predicted and ground truth values. Note that because E, Max Strain, and Ultimate Stress span orders of magnitudes, we compare them on the log scale. Generally, the GNN and ANN multi-task and multi-fidelity models have the highest performance, with both models exhibiting the first or second best RMSE and r^2 for every property except for cure time. The GNN-based model shows an advantage for scaling multitask thermoset informatics through the learned combination of the network components. Additionally, across nearly all target properties, the multitask models outperform or are comparable to their single-task baseline counterpart, highlighting the value of jointly training across multiple data sources during training. The multitask GNN achieves consistently r^2 stronger performance for T_g from 0.107 to 0.564 and for cure temperature from 0.323 to 0.439 while maintaining competitive performance on other mechanical properties. Similar trends are seen for the ANN, where the RMSE for E decreases from 1.3 to 0.51 log MPa when trained on external experimental data. Given that different properties arise from distinct underlying mechanisms captured by the fingerprint combinations, the optimal representation may vary. For example, E seems to be better mapped from a linear combination, whereas T_g is better mapped from a learned aggregation via the GNN. A caveat of the MF approach is the potential introduction of conflicting signals from heterogeneous data sources. This is particularly evident for elongation at break, where the inclusion of external data increases the best RMSE from 0.328 to 0.339 log mm/mm for the GNN model, suggesting that data inconsistency can outweigh the benefits of increased sample size. The joint MF and MT model performance is marginally improved for all other properties. The 10-fold held-out data with the lowest RMSE and highest r^2 values are shown in **Figure 4a-f**, and the best area under the receiver operator characteristic curve is 0.88. These benchmarks are only based on the data collected to date, and will change as more data is added through use of the automated lab.

To assess the utility of MD simulations for thermoset T_g with compositions that overlapped with the same compositions used in experiments, we also conducted an assessment of the prediction of T_g with variable amounts of MD data. We run 5 10-fold cross validation splits with varied sampling of MD data. In these low-data regimes, performance depends critically on which data points are sampled. In **Figure 4h**, we find that the distribution of RMSEs decreases from a mean of 41.8 at 0% and 36.53 at 10% of the MD data to 34.47 K at 100%. These results demonstrate opportunities for further model improvement through strategic incorporation of MD simulation data.

3.4 On-Demand Automated Discovery of Thermosets

The goal of this work is to discover new materials using the database and ML models built from thermoset database. Therefore, we implemented the automated discovery framework that builds on the above discussed pipeline to enable efficient optimization of formulations in a larger, flexible chemical design space and across multiple objectives. We explore a two-part optimization scheme. The first part is a Bayesian approach using a GPR surrogate model to evaluate a discretized and constrained formulation space. The second part involves using the GNN MT MF model for gradient-based optimization from a starting formulation that is chosen by the Bayesian approach. This hierarchical approach allows the BO approach to constrain to high-priority areas after enumeration of the full design space, and the gradient optimization with the more accurate GNN enables continuous search over the local compositional simplex. Additionally, properties of materials over the full design space can be viewed as non-convex, and direct optimization is difficult in this setting. By starting in an already constrained part of the manifold, we can more easily find a non-local optimum.

Our design space for the automated system contains five monomers: isodecyl acrylate (IDA), isobornyl acrylate (IBOA), 2-[[(butylamino)carbonyl]oxy]ethyl acrylate (BCOE), benzyl methacrylate (BMA), and 2-hydroxyethyl acrylate (2-HEA); and four crosslinkers: poly(ethylene glycol) diacrylate at sizes 250 and 700 (PEGDA-250, PEGDA-700), di(ethylene glycol) dimethacrylate (DEGDMA), and trimethylolpropane ethoxylate triacrylate (ETPTA). From these, our goal was to design a formulation with at most 2 monomers and 1 crosslinker. Adding more components beyond this yields diminishing returns for realizability and diversity in properties. To create an initial dataset of samples and properties we conducted an exploration of the design space for 18 iterations using diversity and uncertainty acquisition.[44] Because the exploration phase has now established broad coverage of the design space, future optimization cycles can proceed directly without repeating this step. As the dataset continues to grow over future optimization campaigns, model accuracy will likely increase (see Supplementary Information Section 4), enabling faster and more reliable optimization in subsequent iterations.

Following the exploration phase, we target an elastomeric material which balances strength and flexibility with a moderate stiffness of E=1.2 MPa and an UTS/E ratio of > 3, a high elongation at break $\varepsilon > 200\%$, and low curing time of $< 5s$ and temperature of $< 343K$. In the early iterations, we use a Bayesian approach with a GPR surrogate. As more formulations are added to the dataset and neural network–based models improve, we can transition to a gradient-based optimization for higher precision and accuracy multi-task learning. **Figure 5b** shows the regret of the best sample acquired from the desired target. Once the Bayesian approach over an enumerated design space plateaus, applying gradient-based refinement to the selected candidate compositions enables the discovery of formulations with lower regret. In this particular case, the Bayesian optimization recommendation of 85.0% BCOE and 15.0% DEGDMA was refined into a final formulation of 87.4% BCOE and 12.6% DEGDMA using the gradient method, resulting in about a 4 order of magnitude drop in regret. **Figure 5a** shows highlights the specific ranges for each target. Here, we achieved final property values of E=1.198 MPa, UTS=3.7MPa (UTS/E = 3.09), and Elongation at break = 200.9%. In **Figure 5c**, the discovered formulation was printed as a slab and cyclically elongated to 150% strain. Lattice and gyroid structures were also fabricated and evaluated under cyclic compressive loading. In both the gyroid and BCC geometries, the material exhibited minimal changes in hysteresis in the force vs. displacement response after 10 compression cycles, indicating stable mechanical behavior. A video of compression testing of these lattice structures is provided in Supplementary Information (**Movie S4).** The complete end-to-end optimization was accomplished within 18 hours of active experimental time, demonstrating a scalable framework for efficiently identifying formulations that satisfy stringent multi-property targets without exhaustive experimental screening.

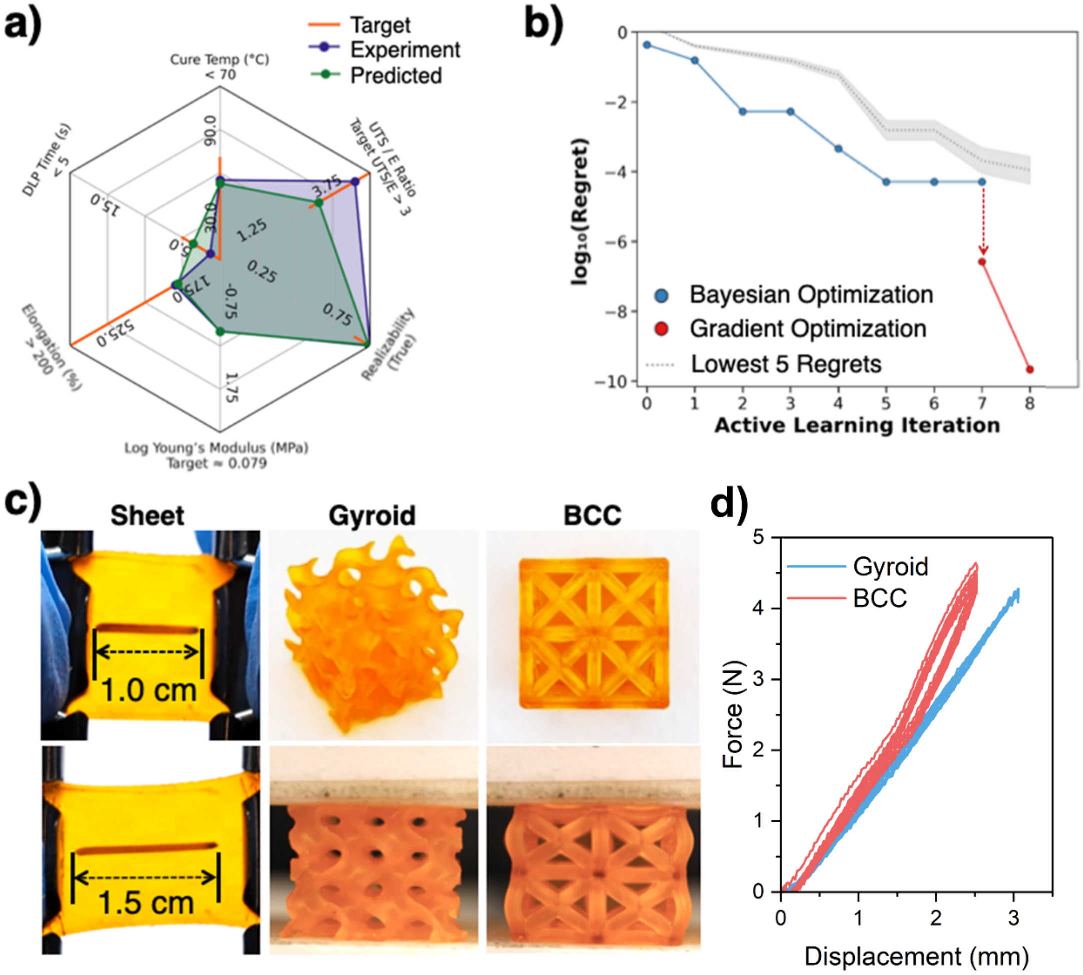

Figure 5. Results of automated materials discovery using the self-driving lab and the informatics protocols developed in this study. a) A radar plot showing the properties of the optimized material composition. b) The log-scaled regret of the best acquired sample after each iteration, first when using Bayesian Optimization and then further optimizing with gradient optimization when sufficient data was acquired. The distribution of the lowest 5 regrets in the dataset is shown across the iterations. c) Demonstrated printability and elastomeric responses of a thin sheet (left), gyroid (center), and BCC (right) structures. d) A demonstration of the cyclic compressive response is shown for the gyroid (3.0 mm displacement) and BCC (2.5 mm displacement) structures.

4 Conclusion

We present an integrated framework for informatics-driven and automated discovery of thermoset acrylates by coupling machine learning–based surrogate models with a self-driving laboratory (SDL) for formulation and characterization workflows in a closed-loop system. The SDL accelerates data generation and enables iterative optimization, achieving more than a 90% reduction in human effort per discovery cycle while reducing the discovery timeline from months to days. By prioritizing experiments through model-guided selection, the framework also minimizes material waste by reducing the total number of required experiments. Another key component of the approach is the unification of diverse data sources through multitask and multi-fidelity learning, combining simulations, literature data, and experiments to improve model generalization and predictive accuracy for downstream optimization. We further demonstrate that simulated T_g correlate with experimental T_g across varying chemistries and conversion rates, suggesting that future integration of simulated T_g into the active learning loop could accelerate optimization through additional multifidelity signals. Together with expanded automated characterization capabilities for T_g, this framework represents an important step toward breaking the traditional trial-and-error cycle in 3D printing material development and advancing scalable, autonomous materials discovery. Automated characterization of T_g can also enable high throughput experimentation. Ultimately, this work represents a crucial step into breaking the constant experimentation loop within 3D printing material design. The convergence of informatics, automation, and multi-source learning paves the way for an era of truly autonomous, intelligent materials design, transforming how functional materials are developed for next-generation manufacturing applications.

5 Acknowledgement

Authors acknowledges A. Savit for help with polyBART fingerprinting, and S. Shukla for valuable discussions on molecular dynamics simulations. The support from an NSF grant (CMMI-2323695) is gratefully acknowledged.

6 References

1 Armstrong, C. D., Yue, L., Demoly, F., Zhou, K. & Qi, H. J. Unstructured Direct Ink Write 3D Printing of Functional Structures with Ambient Temperature Curing Dual-Network Thermoset Ink. *Advanced Intelligent Systems* **5**, 2200226 (2023). https://doi.org/https://doi.org/10.1002/aisy.202200226

2 Chen, K., Kuang, X., Li, V., Kang, G. & Qi, H. J. Fabrication of tough epoxy with shape memory effects by UV-assisted direct-ink write printing. *Soft Matter* **14**, 1879-1886 (2018). https://doi.org/10.1039/C7SM02362F

3 Bourell, D. *et al.* Materials for additive manufacturing. *CIRP Annals* **66**, 659-681 (2017). https://doi.org/https://doi.org/10.1016/j.cirp.2017.05.009

4 Safranski, D. L. & Gall, K. Effect of chemical structure and crosslinking density on the thermo-mechanical properties and toughness of (meth)acrylate shape memory polymer networks. *Polymer* **49**, 4446-4455 (2008). https://doi.org/https://doi.org/10.1016/j.polymer.2008.07.060

5 Van de Voorde, K. M., Kozawa, S. K., Mack, J. A. & Thompson, C. B. Influence of Cross-Linker Functionality and Photoinitiator Loading on Network Connectivity and Actuation in 3D-Printed Model Thermosets. *ACS Applied Polymer Materials* **6**, 3918-3929 (2024). https://doi.org/10.1021/acsapm.3c03217

6 Erps, T. *et al.* Accelerated discovery of 3D printing materials using data-driven multiobjective optimization. *Science Advances* **7**, eabf7435 https://doi.org/10.1126/sciadv.abf7435

7 Doan Tran, H. *et al.* Machine-learning predictions of polymer properties with Polymer Genome. *Journal of Applied Physics* **128**, 171104 (2020). https://doi.org/10.1063/5.0023759

8 Gurnani, R., Kuenneth, C., Toland, A. & Ramprasad, R. Polymer Informatics at Scale with Multitask Graph Neural Networks. *Chemistry of Materials* **35**, 1560-1567 (2023). https://doi.org/10.1021/acs.chemmater.2c02991

9 Kuenneth, C., Schertzer, W. & Ramprasad, R. Copolymer Informatics with Multitask Deep Neural Networks. *Macromolecules* **54**, 5957-5961 (2021). https://doi.org/10.1021/acs.macromol.1c00728

10 Shukla, S. S., Kuenneth, C. & Ramprasad, R. Polymer informatics beyond homopolymers. *MRS Bulletin* **49**, 17-24 (2024). https://doi.org/10.1557/s43577-023-00561-0

11 Jain, A., Armstrong, C. D., Joseph, V. R., Ramprasad, R. & Qi, H. J. Machine-Guided Discovery of Acrylate Photopolymer Compositions. *ACS Applied Materials & Interfaces* **16**, 17992-18000 (2024). https://doi.org/10.1021/acsami.4c00759

12 Tom, G. *et al.* Self-Driving Laboratories for Chemistry and Materials Science. *Chemical Reviews* **124**, 9633-9732 (2024). https://doi.org/10.1021/acs.chemrev.4c00055

13 Zhu, S. *et al.* Differentiable modeling and optimization of non-aqueous Li-based battery electrolyte solutions using geometric deep learning. *Nature Communications* **15**, 8649 (2024). https://doi.org/10.1038/s41467-024-51653-7

14 Szymanski, N. J. *et al.* An autonomous laboratory for the accelerated synthesis of inorganic materials. *Nature* **624**, 86-91 (2023). https://doi.org/10.1038/s41586-023-06734-w

15 Quinn, H. *et al.* PANDA: a self-driving lab for studying electrodeposited polymer films. *Materials Horizons* **11**, 5331-5340 (2024). https://doi.org/10.1039/D4MH00797B

16 Phan, B. K. *et al.* Gas permeability, diffusivity, and solubility in polymers: Simulation-experiment data fusion and multi-task machine learning. *npj Computational Materials* **10**, 186 (2024). https://doi.org/10.1038/s41524-024-01373-9

17 Venkatram, S. *et al.* Predicting Crystallization Tendency of Polymers Using Multifidelity Information Fusion and Machine Learning. *The Journal of Physical Chemistry B* **124**, 6046-6054 (2020). https://doi.org/10.1021/acs.jpcb.0c01865

18 Gholami, F. *et al.* Fast and Efficient Fabrication of Functional Electronic Devices through Grayscale Digital Light Processing 3D Printing. *Advanced Materials* **36**, 2408774 (2024). https://doi.org/https://doi.org/10.1002/adma.202408774

19 Abolhasani, M. & Kumacheva, E. The rise of self-driving labs in chemical and materials sciences. *Nature Synthesis* **2**, 483-492 (2023). https://doi.org/10.1038/s44160-022-00231-0

20 Burger, B. *et al.* A mobile robotic chemist. *Nature* **583**, 237-241 (2020). https://doi.org/10.1038/s41586-020-2442-2

21 Wu, J. *et al.* Evolution of material properties during free radical photopolymerization. *Journal of the Mechanics and Physics of Solids* **112**, 25-49 (2018). https://doi.org/https://doi.org/10.1016/j.jmps.2017.11.018

22 ASTM. in *ASTM D638-14* (2022).

23 Bradski, G. The opencv library. *Dr. Dobb's Journal: Software Tools for the Professional Programmer* **25**, 120-123 (2000).

24 Huang, W. & Jing, Z. Evaluation of focus measures in multi-focus image fusion. *Pattern Recognition Letters* **28**, 493-500 (2007). https://doi.org/https://doi.org/10.1016/j.patrec.2006.09.005

25 Mannodi-Kanakkithodi, A. *et al.* Scoping the polymer genome: A roadmap for rational polymer dielectrics design and beyond. *Materials Today* **21**, 785-796 (2018). https://doi.org/https://doi.org/10.1016/j.mattod.2017.11.021

26 Kuenneth, C. & Ramprasad, R. polyBERT: a chemical language model to enable fully machine-driven ultrafast polymer informatics. *Nature Communications* **14**, 4099 (2023). https://doi.org/10.1038/s41467-023-39868-6

27 Savit, A., Sahu, H., Shukla, S., Xiong, W. & Ramprasad, R. polyBART: A Chemical Linguist for Polymer Property Prediction and Generative Design. *arXiv preprint arXiv:2506.04233* (2025).

28 Goodall, R. E. A. & Lee, A. A. Predicting materials properties without crystal structure: deep representation learning from stoichiometry. *Nature Communications* **11**, 6280 (2020). https://doi.org/10.1038/s41467-020-19964-7

29 Brooks, B. R. *et al.* CHARMM: The biomolecular simulation program. *Journal of Computational Chemistry* **30**, 1545-1614 (2009). https://doi.org/https://doi.org/10.1002/jcc.21287

30 Van Der Spoel, D. *et al.* GROMACS: Fast, flexible, and free. *Journal of Computational Chemistry* **26**, 1701-1718 (2005). https://doi.org/https://doi.org/10.1002/jcc.20291

31 Huang, M. & Abrams, C. F. HTPolyNet: A general system generator for all-atom molecular simulations of amorphous crosslinked polymers. *SoftwareX* **21**, 101303 (2023). https://doi.org/https://doi.org/10.1016/j.softx.2022.101303

32 Patrone, P. N., Dienstfrey, A., Browning, A. R., Tucker, S. & Christensen, S. Uncertainty quantification in molecular dynamics studies of the glass transition temperature. *Polymer* **87**, 246-259 (2016). https://doi.org/https://doi.org/10.1016/j.polymer.2016.01.074

33 Lookman, T., Balachandran, P. V., Xue, D. & Yuan, R. Active learning in materials science with emphasis on adaptive sampling using uncertainties for targeted design. *npj Computational Materials* **5**, 21 (2019). https://doi.org/10.1038/s41524-019-0153-8

34 Smith, K. E., Temenoff, J. S. & Gall, K. On the toughness of photopolymerizable (meth) acrylate networks for biomedical applications. *Journal of applied polymer science* **114**, 2711-2722 (2009).

35 Smith, K. E., Parks, S. S., Hyjek, M. A., Downey, S. E. & Gall, K. The effect of the glass transition temperature on the toughness of photopolymerizable (meth)acrylate networks under physiological conditions. *Polymer* **50**, 5112-5123 (2009). https://doi.org/https://doi.org/10.1016/j.polymer.2009.08.040

36 Anastasio, R., Cardinaels, R., Peters, G. W. M. & van Breemen, L. C. A. Structure–mechanical property relationships in acrylate networks. *Journal of Applied Polymer Science* **137**, 48498 (2020). https://doi.org/https://doi.org/10.1002/app.48498

37 Anastasio, R., Peerbooms, W., Cardinaels, R. & van Breemen, L. C. A. Characterization of Ultraviolet-Cured Methacrylate Networks: From Photopolymerization to Ultimate Mechanical Properties. *Macromolecules* **52**, 9220-9231 (2019). https://doi.org/10.1021/acs.macromol.9b01439

38 Lecamp, L., Youssef, B., Bunel, C. & Lebaudy, P. Photoinitiated polymerization of a dimethacrylate oligomer: 1. Influence of photoinitiator concentration, temperature and light intensity. *Polymer* **38**, 6089-6096 (1997). https://doi.org/https://doi.org/10.1016/S0032-3861(97)00184-5

39 Kannurpatti, A. R., Anderson, K. J., Anseth, J. W. & Bowman, C. N. Use of “living” radical polymerizations to study the structural evolution and properties of highly crosslinked polymer networks. *Journal of Polymer Science Part B: Polymer Physics* **35**, 2297-2307 (1997). https://doi.org/https://doi.org/10.1002/(SICI)1099-0488(199710)35:14<2297::AID-POLB10>3.0.CO;2-7

40 Sideridou, I., Tserki, V. & Papanastasiou, G. Study of water sorption, solubility and modulus of elasticity of light-cured dimethacrylate-based dental resins. *Biomaterials* **24**, 655-665 (2003). https://doi.org/https://doi.org/10.1016/S0142-9612(02)00380-0

41 Kannurpatti, A. R., Anseth, J. W. & Bowman, C. N. A study of the evolution of mechanical properties and structural heterogeneity of polymer networks formed by photopolymerizations of multifunctional (meth)acrylates. *Polymer* **39**, 2507-2513 (1998). https://doi.org/https://doi.org/10.1016/S0032-3861(97)00585-5

42 Afzal, M. A. F. *et al.* High-Throughput Molecular Dynamics Simulations and Validation of Thermophysical Properties of Polymers for Various Applications. *ACS Applied Polymer Materials* **3**, 620-630 (2021). https://doi.org/10.1021/acsapm.0c00524

43 Li, C. & Strachan, A. Molecular scale simulations on thermoset polymers: A review. *Journal of Polymer Science Part B: Polymer Physics* **53**, 103-122 (2015). https://doi.org/https://doi.org/10.1002/polb.23489

44 Zhdanov, F. Diverse mini-batch active learning. *arXiv preprint arXiv:1901.05954* (2019).

Supplementary information for:

Scalable Thermoset Informatics and On-Demand Discovery through Autonomous Experimentation

Marcus R. Fratarcangeli,[1†] Ayush Jain,[2,3†] Farzad Gholami,[1,2†] Jiaqi Nie,[1] H. Jerry Qi,[1*] and Rampi Ramprasad[2*]

[1]School of Mechanical Engineering, Georgia Institute of Technology, Atlanta, GA 30332, United States

[2]School of Materials Science and Engineering, Georgia Institute of Technology, Atlanta, GA 30332, United States

[3]School of Computational Science and Engineering, Georgia Institute of Technology, Atlanta, GA 30332, United States

[†]Equal Contribution First Authors

*Corresponding authors, HJQ, qih@me.gatech.edu; RR, rampi.ramprasad@mse.gatech.edu

7 Acrylate Monomers in *ThermosetDB*

Table S4.List of monomers with acronyms and SMILES

Name	Acronym	SMILES
Glycidyl Methacrylate	GMA	`CC(=C)C(=O)OCC1CO1`
Isobornyl acrylate	IBOA	`[H][C@]12CC[C@@](C)([C@@H](C1)OC(=O)C=C)C2(C)C`
Butyl Acrylate	BA	`CCCCOC(=O)C=C`
2-Hydroxyethyl acrylate	2-HEA	`C=CC(=O)OCCO`
2-Hydroxyethyl methacrylate	2-HEMA	`CC(=C)C(=O)OCCO`
Acrylic acid	AA	`C=CC(=O)O`
Isodecyl acrylate	IDA	`CC(C)CCCCCCCOC(=O)C=C`
2-Ethoxyethyl methacrylate	2-EEMA	`CCOCCOC(=O)C(C)=C`
tert-Butyl Acrylate	t-BA	`CC(C)(C)OC(=O)C=C`
Benzyl methacrylate	BMA	`CC(=C)C(=O)OCc1ccccc1`
2-[[(Butylamino)carbonyl]oxy]ethyl acrylate	BCOE	`CCCCNC(=O)OCCOC(=O)C=C`
Poly-ethylene Glycol Diacrylate	PEGDA	`C=CC(=O)OCCOCCOCCOC(=O)C=C`
Bisphenol A ethoxylate diacrylate	BPAEDA-500	`C=CC(=O)OCCOCC(C)(c1ccc(O)cc1)c2ccc(O)cc2OCCOCCOC(=O)C=C`
Bisphenol A ethoxylate diacrylate	BPAEDA-700	`C=CC(=O)OCCOCCOCCOCCOCC(C)(c1ccc(O)cc1)c2ccc(O)cc2OCCOCCOCCOCCOC(=O)C=C`
Trimethylolpropane ethoxylate triacrylate	ETPTA	`CCC(COCCOC(=O)C=C)(COCCOC(=O)C=C)COCCOC(=O)C=C`
Ethylene glycol phenyl ether acrylate	PA	`C=CC(=O)OCCOc1ccccc1`
2-(Diethylamino)ethyl methacrylate	DEAEMA	`CCN(CC)CCOC(=O)C(C)=C`
Poly-ethylene Glycol Diacrylate 575	PEG-575	`C=CC(=O)OCCOCCOCCOCCOCCOCCOCCOCCOCCOCCOC(=O)C=C`
Poly-ethylene Glycol Diacrylate 700	PEG-700	`C=CC(=O)OCCOCCOCCOCCOCCOCCOCCOCCOCCOCCOCCOCCOCCOC(=O)C=C`
Poly-ethylene Glycol Diacrylate 300	PEGDMA-300	`C=CC(=O)OCCOCCOCCOCCOC(=O)C=C`
Di(ethylene glycol) dimethacrylate	DEGDMA	`CC(=C)C(=O)OCCOCCOC(=O)C(C)=C`
Aliphatic Urethane Diacrylate	AUD	`C=CC(=O)OCOC(=O)NCNC(=O)OCOC(=O)C=C`
Poly(ethylene glycol) dimethacrylate	PEGDMA	`C=C(C)C(=O)OCCOCCOCCOCCOCCOCCOCCOCCOCCOC(=O)C(=C)C`
Methyl acrylate	MA	`COC(=O)C(C)=C`
Methyl methacrylate	MMA	`COC(=O)C(C)=C`
tert-Butyl methacrylate	tBMA	`CC(=C)C(=O)OC(C)(C)C`
Isobornyl methacrylate	IMA	`CC(=C)C(=O)OC1C[C@H]2CC[C@]1(C)C2(C)C`
2-Ethylhexyl methacrylate	2EHM	`CCCCCC(CC)COC(=O)C(C)=C`
Ethylene glycol phenyl ether methacrylate	EGPEM	`CC(=C)C(=O)OCCOc1ccccc1`
Poly(propylene glycol) acrylate	PPGA	`C=CC(=O)OCC(C)OCC(C)OCC(C)OCC(C)OCC(C)OCC(C)OCC(C)O`
Poly(ethylene glycol) phenyl ether acrylate (Mn 236)	PEGPEA236	`C=CC(=O)OCCOCCOc1ccccc1`
Poly(ethylene glycol) phenyl ether acrylate (Mn 280)	PEGPEA280	`C=CC(=O)OCCOCCOCCOc1ccccc1`
Poly(ethylene glycol) phenyl ether acrylate (Mn 324)	PEGPEA324	`C=CC(=O)OCCOCCOCCOCCOc1ccccc1`
Benzyl acrylate	BZA	`O(Cc1ccccc1)C(=O)C=C`
Bisphenol A ethoxylate diacrylate Mn 688	BPA688	`C=CC(=O)OCCOCCOCCOc1ccc(cc1)C(C)(C)c2ccc(cc2)OCCOCCOCCOCCOC(=O)C=C`
Bisphenol A ethoxylate diacrylate Mn 468	BPA468	`C=CC(=O)OCCOCCOc1ccc(cc1)C(C)(C)c2ccc(cc2)OCCOC(=O)C=C`
1,6-Hexanediol diacrylate	HEXDA	`C=CC(=O)OCCCCCCOC(=O)C=C`
Trimethylolpropane ethoxylate triacrylate Mn 604	TETA604	`C=CC(=O)OCCOCCOCCOCC(CC)(COCCOCCOC(=O)C=C)COCCOCCOC(=O)C=C`
Trimethylolpropane ethoxylate triacrylate Mn 912	TETA912	`C=CC(=O)OCCOCCOCCOCCOCCOCC(CC)(COCCOCCOCCOCCOC(=O)C=C)COCCOCCOCCOCCOCCOC(` `=O)C=C`
Glycerol propoxylate triacrylate	GPTA	`C=CC(=O)OCCCOCC(COCCCOC(=O)C=C)OCCCOC(=O)C=C`
Di(trimethylolpropane) tetraacrylate	DTTA	`CCC(COCC(CC)(COC(=O)C=C)COC(=O)C=C)(COC(=O)C=C)COC(=O)C=C`
Dipentaerythritol penta/hexaacrylate	DPPHA	`C=CC(=O)OCC(CO)(COCC(COC(=O)C=C)(COC(=O)C=C)COC(=O)C=C)COC(=O)C=C`
Poly-ethylene Glycol Diacrylate 700	PEGDMA750	`C=C(C)C(=O)OCCOCCOCCOCCOCCOCCOCCOCCOCCOCCOCCOCCOCCOC(=O)C(=C)C`
Bisphenol A ethoxylate dimethacrylate Mn 1700	BPA1700	`C=C(C)C(=O)OCCOCCOCCOCCOCCOCCOCCOCCOCCOCCOCCOCCOCCOCCOCCOc1ccc(cc1)C(C)(C` `)c2ccc(cc2)OCCOCCOCCOCCOCCOCCOCCOCCOCCOCCOCCOCCOCCOCCOCCOC(=O)C(C)=C`
Bisphenol A ethoxylate dimethacrylate Mn 540	BPA540	`C=C(C)C(=O)OCCOCCOc1ccc(cc1)C(C)(C)c2ccc(cc2)OCCOCCOC(=O)C(C)=C`
Octyl Methacrylate	OctMA	`CCCCCCCCOC(=O)C(=C)C`
Heptyl Methacrylate	HepMA	`CCCCCCCCOC(=O)C(=C)C`
Diethylene glycol diacrylate	PEGDA-2	`C=CC(=O)OCCOCCOC(=O)C=C`
Pentaerythritol Tetracrylate	PETA	`C=CC(=O)OCC(COC(=O)C=C)(COC(=O)C=C)COC(=O)C=C`
2,2-bis[4(2,3-hydroxypropoxy)phenyl]propane	Bis-HPPP	`CC(C1=CC=C(OCC(O)COC(C(C)=C)=O)C=C1)(C2=CC=C(OCC(O)COC(C(C)=C)=O)C=C2)C`
Triethylene glycol dimethacrylate	TEGDMA	`C=C(C)C(=O)OCCOCCOCCOC(=O)C(=C)C`
Poly-ethylene Glycol Diacrylate 600	PEGDMA-600	`C=C(C)C(=O)OCCOCCOCCOCCOCCOCCOCCOCCOCCOCCOC(=O)C(=C)C`
Neopentyl glycol propoxylate diacrylate	NGPDA	`C=CC(=O)OCCCOCC(C)(C)COCCCOC(=O)C=C`
Trimethylolpropane propoxylate triacrylate	TPTA	`C=CC(=O)OCCCOCCCOCC(CC)(COCCCOCCCOC(=O)C=C)COCCCOCCCOC(=O)C=C`
Urethane Dimethacrylate	UDMA	`C=CC(=O)OCCOCCOC(=O)C=CCC(CCNC(=O)OCCOC(=O)C(C)=C)CC(C)(C)CNC(=O)OCCOC(=O` `)C(C)=C`

8 Graph Neural Network Methodology

We adopt a Graph Attention Network (GAT)[1] to learn the relative importance of each monomer in a latent representation of the formulation, given the other monomers and the composition. For each node i, its updated representation at layer ℓ is given by **eq. S1**:

$$h_i^{(l)} =\|_{k=1}^{H} \sigma\left(\sum_{j\in N(i)} \alpha_{ij}^{(l,k)} W^{(l,k)} h_j^{(l-1)}\right) \tag{S1}$$

where $h_i^{(l-1)} \in R^{d_{in}}$ is the input feature of node i, $W^{(l,k)} \in R^{d_{out} \times d_{in}}$ is the learnable projection for head k, H is the number of attention heads, ∥ denotes concatenation across heads, and $\sigma(\cdot)$ is a non-linear activation.

We use one GAT layer because the fully connected graph contains all the connections needed to represent the mixture. Node embeddings $\left\{h_i^{(L)}\right\}$, are aggregated into a graph-level embedding h_G via global mean pooling $h_G = \frac{1}{|V|} \sum_{i \in V} h_i^{(L)}$.

The pooled representation $h_G$is processed through a shared multilayer perceptron (MLP) with a one-hot encoding to extract task-independent features. From this shared embedding z, two separate task-specific heads are applied, with the property $\hat{y}_{property}$ as regression and realizability $\hat{y}_{realizability}$ as classification between 0 and 1. The first head predicts continuous molecular or reaction properties, while the second predicts a realizability score for feasibility classification.

The model is trained in a multi-task setting with a weighted loss:

$$\mathcal{L} = \lambda_{prop} \mathcal{L}_{MSE}\left(\hat{y}_{property}, y_{property}\right) + \lambda_{real} \mathcal{L}_{BCE}\left(\hat{y}_{realizability}, y_{realizability}\right) \tag{S2}$$

where $\mathcal{L}_{MSE}$ denotes mean squared error for regression, $\mathcal{L}_{BCE}$ denotes binary cross-entropy loss, and λ_{prop}, λ_{real} are hyperparameters controlling a weighting between tasks.

9 Hyperbolic Fitting for Glass Transition Temperature Details

The primary fitting function used to model the property-temperature relationship is a hyperbolic function:

$$\rho(T) = \rho_0 - \alpha(T - T_0) - b. H_0(T, T_0, c) \tag{S3}$$

where the hyperbolic component H_0 is defined as:

$$H_0(T, T_0, c) = \frac{1}{2}(T - T_0) + \sqrt{\frac{(T - T_0)^2}{4} + e^c} \tag{S4}$$

The transition probability function is given by:

$$P(T, T_0, c) = \frac{1}{2} + \frac{T - T_0}{2\sqrt{\frac{(T - T_0)^2}{4} + e^c}} \tag{S5}$$

The transition interval is calculated using a cutoff probability (P_{hat}):

$$\Delta T = \frac{e^{\frac{c}{2}}(2P_{hat} - 1)}{\sqrt{P_{hat}(1 - P_{hat})}} \tag{S6}$$

The transition interval bounds are then:

$$T_{low} = T_0 - \Delta T \tag{S7}$$

$$T_{high} = T_0 + \Delta T \tag{S8}$$

where $P_{hat} = 0.8$.

10 Gradient Optimization Details

10.1 Loss Functions

We implement three loss functions, tailored to different optimization scenarios:

Mean Squared Error (MSE): For exact target matching,

$$\mathcal{L}_{MSE}(f(x), t) = (f(x) - t)^2 \tag{S9}$$

Double Hinge Loss: For range-based optimization where $f(x) \in [t_{min}, t_{max}]$,

$$\mathcal{L}_{MSE}(f(x), [t_{min}, t_{max}]) = \begin{cases} 0, & t_{min} \leq f(x) \leq t_{max} \\ \min(|f(x) - t_{min}|, |f(x) - t_{max}|)^2, & otherwise \end{cases} \tag{S10}$$

Single Hinge Loss: For inequality constraints (maximize or minimize),

$$\mathcal{L}_{single}(f(x), t) = \max(0, 1 \mp f(x). t) \tag{S11}$$

10.2 Constraint Handling

To enforce simplex constraints, we use a softmax projection:

$$x_i^{proj} = \frac{\exp(x_i^{raw})}{\sum_{j=1}^{n} \exp(x_j^{raw})} \tag{S12}$$

10.3 Modified Adam Optimizer

We adopt a simplex-aware variant of Adam to ensure $\sum_{i=1}^{n} x_i = 1$. The update rules follow:

$$m_t = \beta_1 m_{t-1} + (1 - \beta_1) g_t \tag{S13}$$

$$v_t = \beta_2 v_{t-1} + (1 - \beta_2) g_t^2 \tag{S14}$$

$$\hat{m}_t = \frac{m_t}{1 - \beta_1^t} \tag{S15}$$

$$\hat{v}_t = \frac{v_t}{1 - \beta_2^t} \tag{S16}$$

$$\Delta x_i = \alpha \frac{\hat{m}_{t,i}}{\sqrt{\hat{v}_{t,i}} + \epsilon} + \frac{\eta_t}{t} N(0,1) \tag{S17}$$

with the last component adjusted to preserve the constraint:

$$\Delta x_n = -\sum_{i=1}^{n-1} \Delta x_i \tag{S18}$$

A decaying noise term η_t/t provides exploratory behavior.

To account for predictive uncertainty, we employ Monte Carlo dropout. The GNN is kept in training mode, and multiple stochastic forward passes are averaged:

$$f_{mean}(x) = \frac{1}{N_{MC}} \sum_{i=1}^{N_{MC}} f_i(x) \tag{S19}$$

where N_{MC} (default: 10) is the number of samples. Gradients are computed with respect to f_{mean}. Sparse compositions are simplified by removing components with $x_i < 0.001$, along with their associated edges:

$$\varepsilon' = \{(i,j) \in \varepsilon : x_i > 0.001 \; and \; x_j > 0.001\} \tag{S20}$$

To mitigate local minima, we employ multi-start optimization. We run multiple starts with noise added to the sample from the Bayesian optimization.

Convergence is declared when

$$|\mathcal{L}_t - \mathcal{L}_{t-1}| < \tau, \qquad \tau = 10^{-6} \tag{S21}$$

To escape local minima, we apply a Dirichlet kick:

$$x_{new} = (1 - \lambda) x_{current} + \lambda x_{Dirichlet} \tag{S22}$$

where $x_{\mathrm{Dirichlet}} \sim \mathrm{Dirichlet}(\kappa x_{\mathrm{current}})$ with $\kappa = 40$ and $\lambda = 0.25$

10.4 Algorithm Summary

The complete optimization procedure is as follows:

1. Start from Bayesian Optimization chosen composition x_0.

2. For each iteration $t = 1, \ldots, T_{max}$:
    a. Enforce constraints: $x_t^{proj} = \prod(x_t)$
    b. Prune graph by removing zero-valued components.
    c. Forward pass through GNN (stochastic if enabled): $f_t = GNN(x_t^{proj})$
    d. Compute multi-objective loss: $\mathcal{L}_t = \sum_k \omega_k \mathcal{L}_k(f_{t,k}, t_k)$.
    e. Backpropagate to obtain gradients g_t.
    f. Update composition with modified Adam.
    g. Check convergence: if converged for the first time, apply Dirichlet kick.
3. Terminate when convergence is achieved, $T_{max} = 1000$ is reached, or $\mathcal{L}_t < \tau$.
4. Return the best composition and its predicted properties.

11 Exploration Active Learning

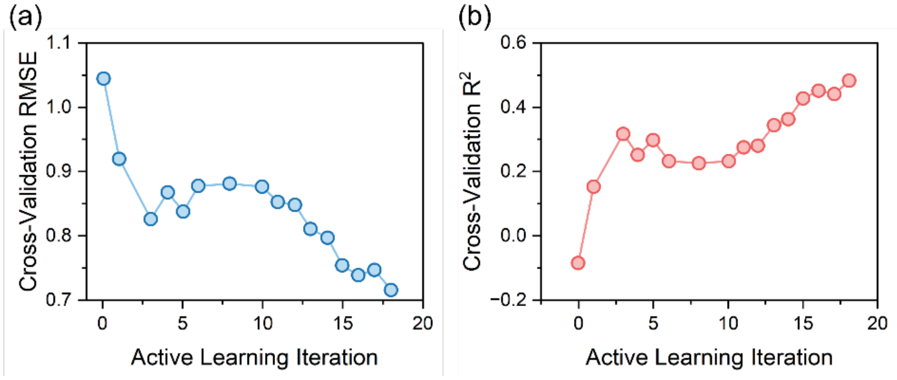

Figure S6. Results of the normalized RMSE and r^2 over several iterations of exploration-based acquisition across the acrylate formulation space.

12 Self-Driving Lab

The SDL lives on a custom-made modular table (Vention, Montreal, CA, USA) that allows for hardware mounting anywhere on the surface. Figure 2 shows a depiction of the SDL table in the lab space and Figure 3 is the top view, showing the real arrangement of different components. The two robots are mounted at either end of the table and face the center, providing them with the largest work area possible. The right robot (Robot 1) manages the MCS and is surrounded by other components: the container dispenser, the cork dispenser, the liquid dispensing system, the powder dispensing system, and the magnetic mixer. The left robot (Robot 2) is responsible for the characterization systems. In front of it is the automated clamp and cameras, then the cleaning stations for the grippers, and to the right is the CTS. Having the systems mounted to the same table allows them to potentially work together in future work. Additions can easily be made to the table to support an additional robot or subsystem to facilitate a completely autonomous SDL.

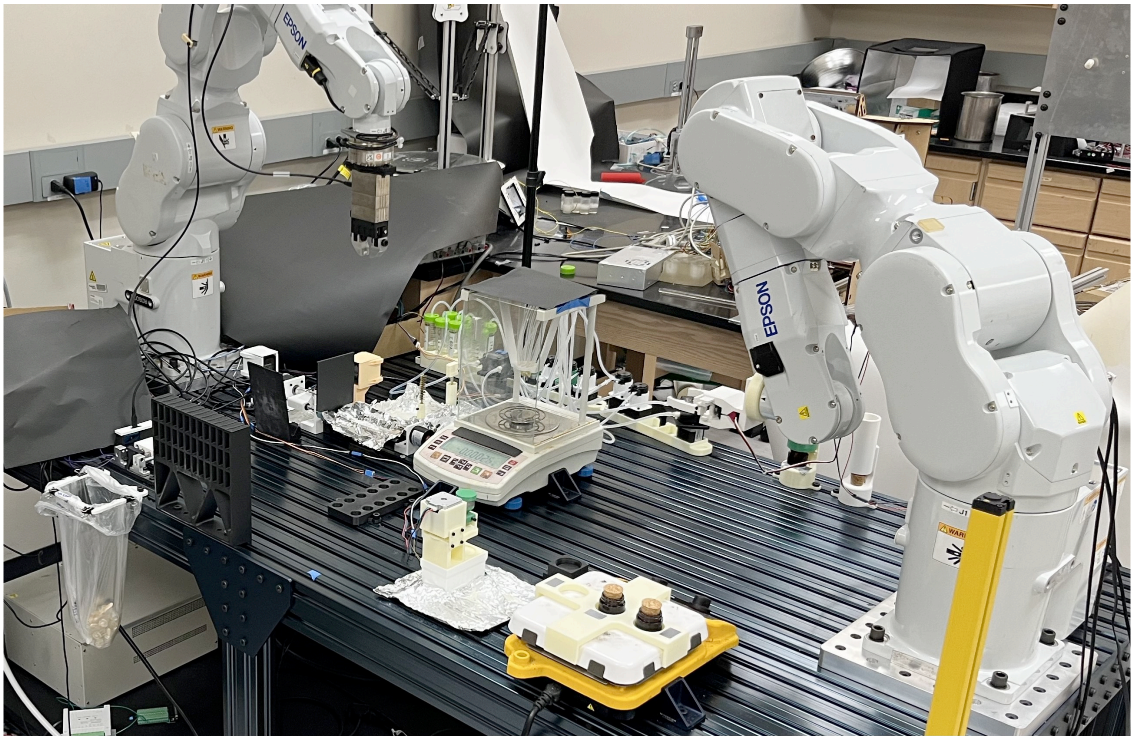

Figure S7. Entire SDL in lab space

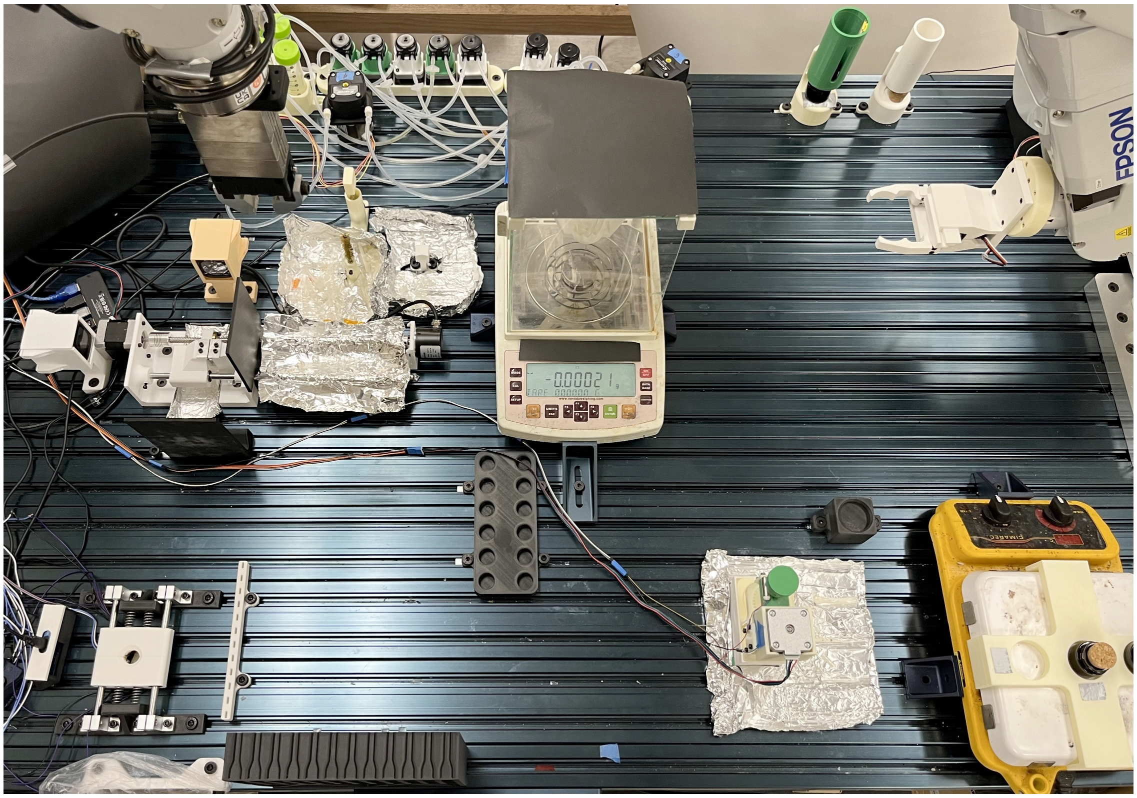

Figure S8. Top view of the SDL mounted to table

The primary CTS hardware is shown in Figure 4, notably the robotic arm with force sensor and gripper, and the ink container/probe tools. The raw data collected from the CTS system are temperature and torque values. An example temperature curve after a single test of a photopolymer ink is demonstrated by Figure 5. The UV light turns on after 30 seconds, and the ink temperature drastically rises as the heat is generated from bonds forming. The temperature then reaches its peak value as it solidifies and slowly begins cooling. The torque acting on the force sensor is measured simultaneously. Each point in Figure 6 represents the normalized amplitude of torque values, given that the gripper is oscillating the probe in the ink. The parameters shown on the plot are relevant to the fitted sigmoidal curve:

$$f = \frac{A}{1 + \exp\left(\frac{x-h}{s}\right)} + C \tag{S23}$$

where A is the parameter for the height of the top line relative to the bottom line, C is for the height of the bottom line, h represents the inflection point, and s is the distance between the top and bottom lines along the abscissa.

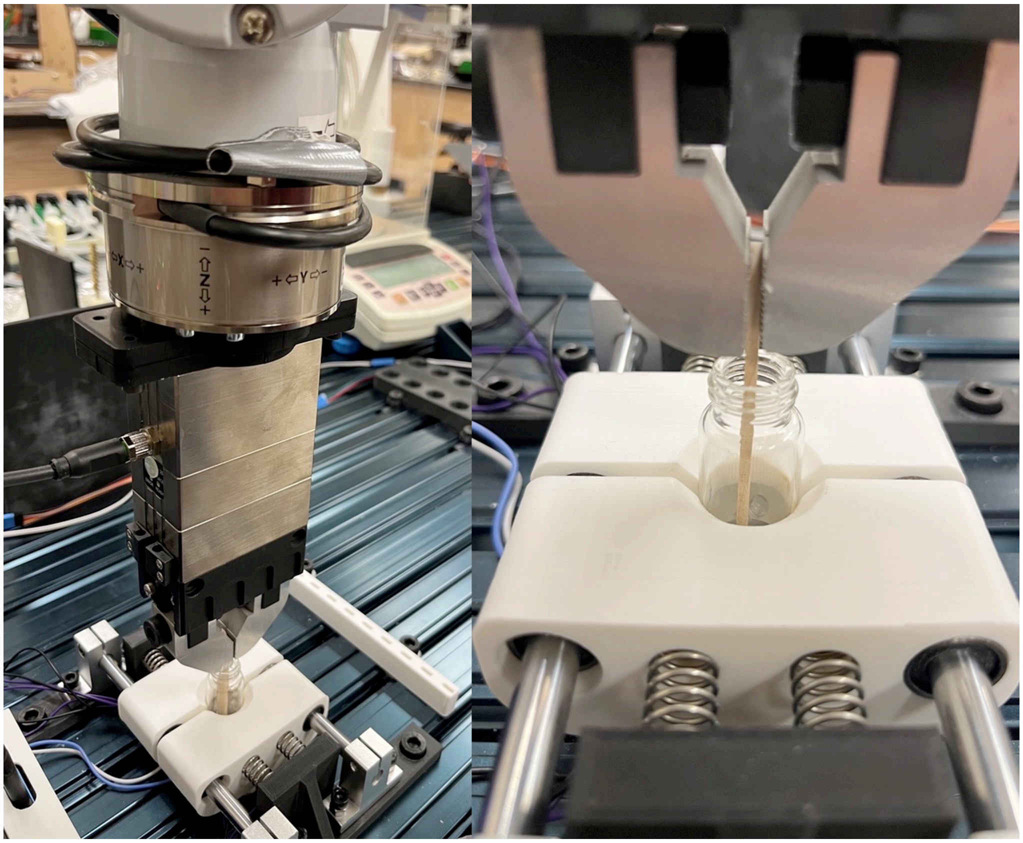

Figure S9. Far and close view of CTS hardware

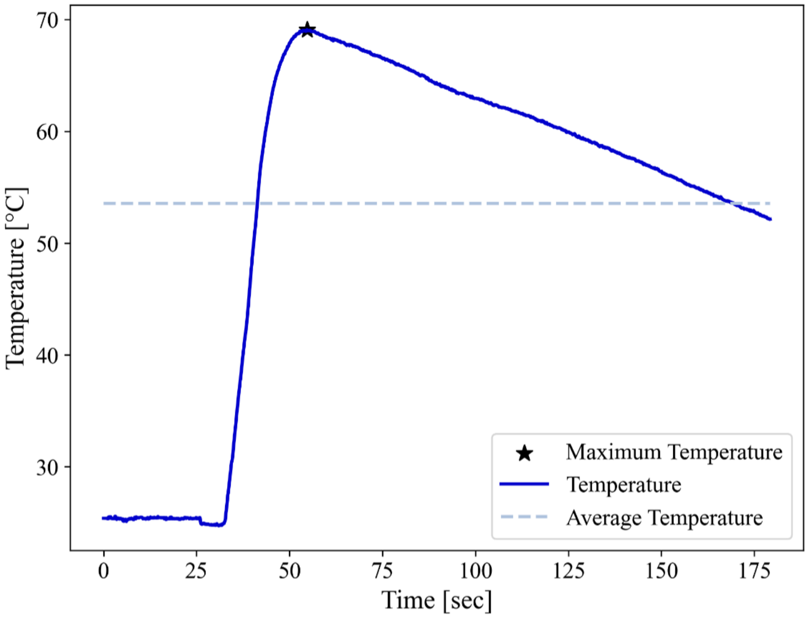

Figure S10. Example temperature curve of a photopolymer ink during CTS test.

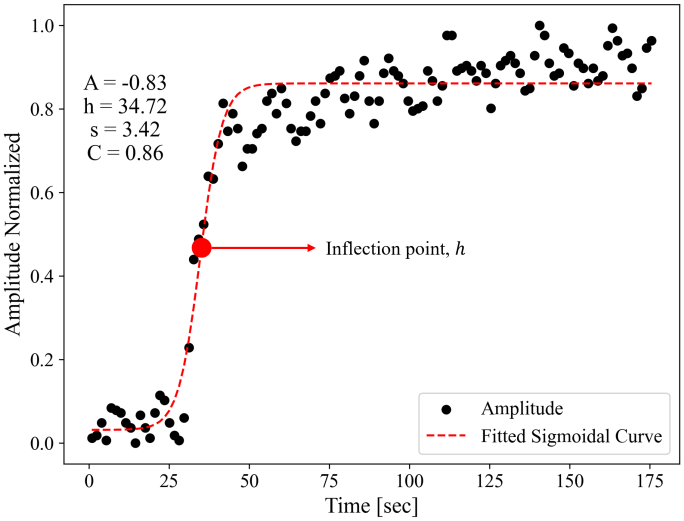

Figure S11. Example torque curve of a photopolymer ink during CTS test

13 References

(1) Velickovic, P.; Cucurull, G.; Casanova, A.; Romero, A.; Lio, P.; Bengio, Y. Graph Attention Networks. International Conference on Learning Representations. 2018.